Supplementary Information

An emerging deep eutectic solvent based on halogen-bond

Ruifen Shi, Dongkun Yu, Fengyi Zhou, Jiangfeng Yu, Tiancheng Mu*

Department of Chemistry, Renmin University of China, Beijing 100872, China. Email: tcmu@ruc.edu.cn; Tel: +86-10-62514925.

Table of Contents

1. Experiment Section

Materials

Tetraethylammonium chloride (TEAC, 98%, CAS no. 56-34-8), tetraethylammonium bromide (TEAB, 98%, CAS no. 71-91-0) and iodine monochloride (ICl, ≥95%, CAS no. 7790-99-0) were purchase from Aladdin Biochemical Technology Co., Ltd (Shanghai, China). Tetrabutylammonium chloride (TBAC, 98%, CAS no. 1112-67-0) was obtained from Saen Chemical Technology Co., Ltd (Shanghai, China). Tetrabutylammonium bromide (TBAB, 99%, CAS no. 1643-19-2) was acquired from Adamas Reagent Co., Ltd. Iodine monobromide (IBr, 98%, CAS no. 7789-33-5) was bought from Alfa Essa (China) Chemical Co., Ltd. All chemicals were used as received without further purification. The melting point of TEAC, TEAB, TBAC and TBAB are 110 ℃, 285 ℃, 83-86 ℃, 105 ℃, respectively, obtained from SciFinder.

Synthesis

In this work, all of the XDESs were prepared just by stirring and heating of the electron acceptors and donors in the appropriate molar ratio at atmospheric pressure by using a magnetic stirrer at a preset temperature. In details, different molar ratios of quaternary ammonium salts and IBr/ICl (1:4, 1:3, 1:2, 2:3, 1:1, 3:2, 2:1, 3:1, 4:1) were used to form the XDESs. The heating temperatures for TEAC/TEAB systems and TBAB/TBAC systems were 80 ℃ and 60 ℃, respectively. All mixtures were mixed at 400 rpm for 2 h until homogeneous and stable transparent brown liquids were formed and then stored in a closed vessel at ambient conditions. Notably, all quaternary ammonium salts need to be placed in a vacuum oven at 100 ℃ for 6 h to dry caused by their hygroscopic property before preparing the XDESs. The water content of the prepared XDESs was determined to be below 100 ppm by Karl Fischer titration.

Characterization

Differential scanning calorimetry (DSC) was performed using a Q2000 DSC (TA

Instruments-Waters LLC, USA) system at a heating rate of 10 °C min^{-1} under nitrogen atmosphere. All the eutectic solvents were run in aluminum hermetic crucibles, which were cooled to -60 °C before heating up to room temperature. The equipment had been calibrated in this temperature range. The FT-IR spectra were recorded on Bruker Tensor 27 IR spectrometer and the sample was prepared by the KBr pellet method in the range of 500 to 4000 cm^{-1}. The UV−vis absorption spectra were recorded by using a spectrophotometer (UV-3600, Shimadzu Corp., Japan), and solution ^{13}C NMR experiments were taken on a Bruker Avance 400 MHz spectrometer. TGA curves were measured by using a TGA Q4000 (PerkinElmer Instruments Inc.) in ramp mode (ramp 10 °C min^{-1} to 400 °C, platinum pan). The Dynamic IR spectroscopy was performed in a closed and water-free environment.

We studied the molecular structures of XDESs using density functional theory (DFT) calculations which were all built with Gaussview 5.0[1] and next optimized with Gaussian 09[2]. The M06-2X was chose due to its higher performance for noncovalent interactions systems. And the def2-SVP basic set was used to optimize the structures[3]. The interaction energies (E_{int}) of complexes A···B were calculated by the equation $E_{int} = E_{(AB)} - E_{(A)} - E_{(B)}$. The values of electrostatic potential including the minima and maxima ($V_{s,min}$ and $V_{s,max}$, respectively) on the XDESs surfaces were evaluated with Multiwfn[4]. For the RDG-based NCI spike and corresponding isosurface plots, they were generated by combining the Multiwfn results with VMD[5]. The search for the bond critical point (BCP) of XB, detailed topological and orbit analysis were also carried out by Multiwfn.

Electrostatic potential expression

The electrostatic potential *V(r)* value at any point r for a molecule could be obtained by the following equation:

$$V(r) = \sum_A \frac{Z_A}{|R_A - r|} - \int \frac{\rho(r')dr'}{|r' - r|}$$

in which Z_A represents the charge on nucleus A located at R_A, and ρ(r′) corresponds to the electronic density of the molecule. Among, the negative regions of Lewis base will attractively interact with the positive regions of halogen atom (so called σ-hole). It has also been verified that the local minimum and maximum electrostatic potential ($V_{s,min}$ and $V_{s,max}$, respectively) are more effective to reveal the features of reactive chemistry between attractive compounds[6].

Noncovalent interaction reduced density gradient (NCI-RDG) expression

The noncovalent interaction reduced density gradient (NCI-RDG), a developed technique, could visualize the noncovalent interactions between two components well. In this case, the NCI descriptor was constructed to represent the weak interactions based on the evaluation of the RDG as a function of electron density (ρ(r)):

$$RDG(r) = \left(2\left(3\pi^2\right)^{1/3}\right)^{-1}\left(\left(|\nabla\rho(r)|\right)/\left(\rho(r)\right)^{4/3}\right)$$

The NCI-RDG analyses could map the interaction regions via RDG isosurface with three distinct colors shown in manuscript. It provides an intuitively way to qualitative assess the attribute and strength of noncovalent interactions[7].

2. Supplementary Figures and Discussion

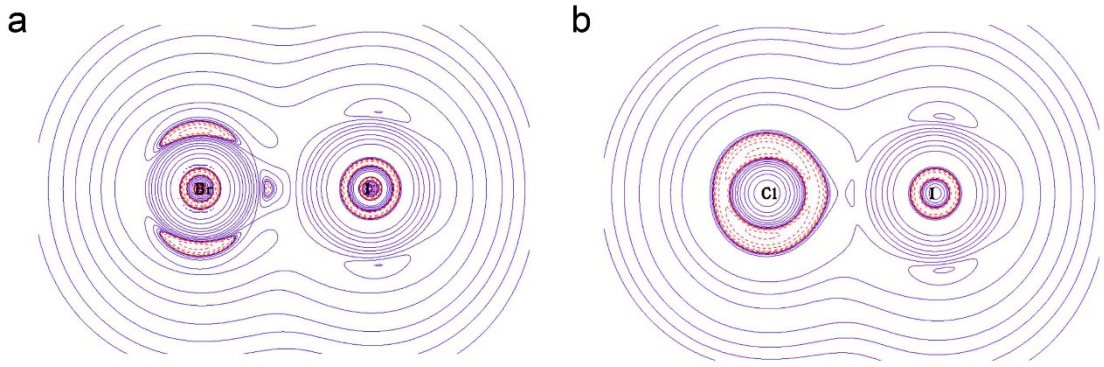

Fig. S1. The 2D contour maps of the Laplacian of the electron density ($\nabla^2\rho$) for XB donors (a) IBr and (b) ICl molecules. The red dash line and purple solid line correspond to the negative and positive zone, respectively. Computational level: M06-2X/def2-SVP.

The topology of the Laplacian of the electron density have been regarded as an effective tool to clarify the XB interaction[8-12]. As shown in Fig. S1a, there are two significant

local concentration of electron density in the valence shell charge concentration of Br. For the ICl molecule, the electrons are concentrated around the whole Cl atom. Compared with Br and Cl, around I atoms belong to a depleted electron density surroundings which can bind the rich-electronic groups to form the XB complex.

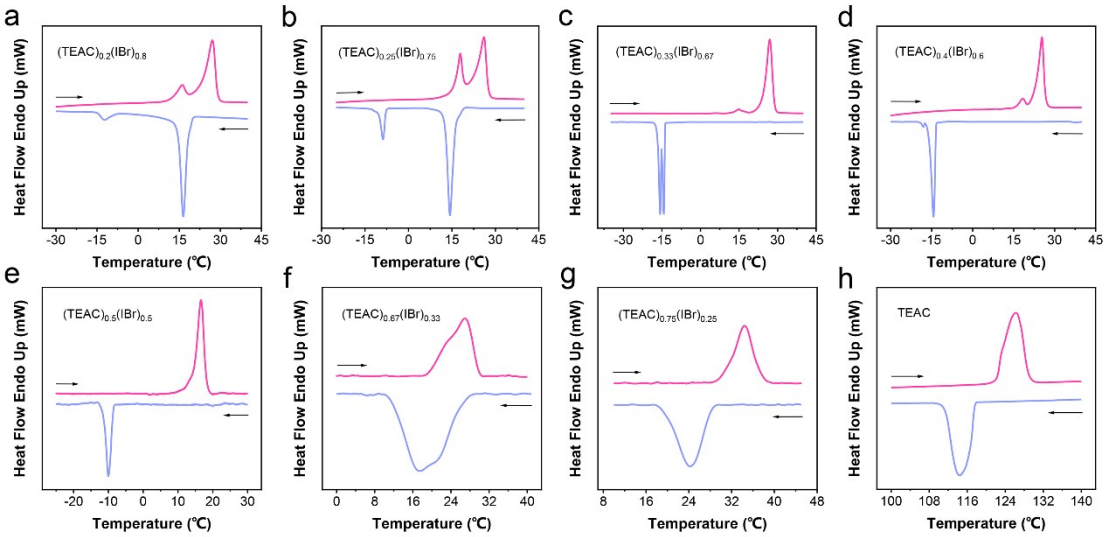

Fig. S2. (a-h) DSC curves of TEAC+IBr system under the different molar ratio. Blue and red lines represent the cooling and heating steps, respectively. The temperature range shown in above figures cover all the appeared peak positions.

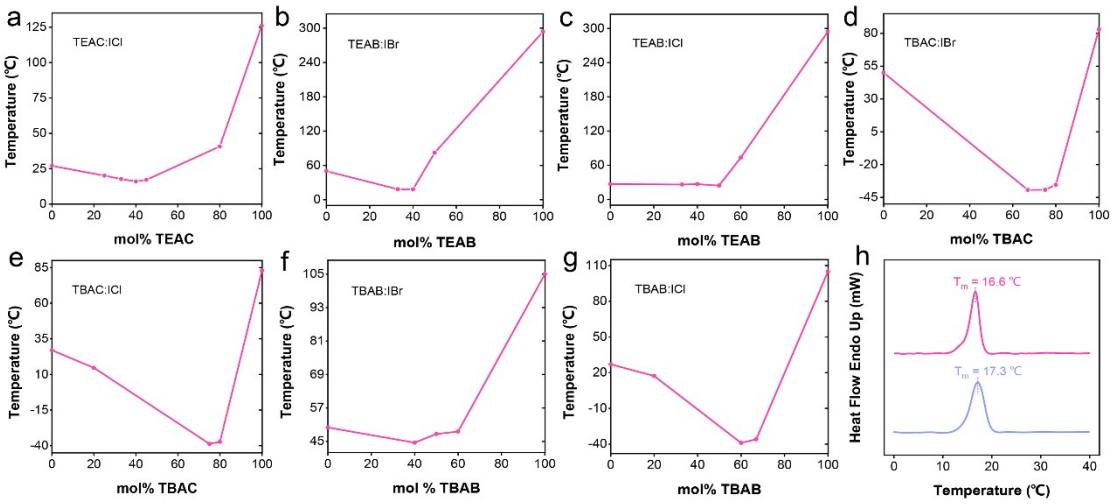

Fig. S3. (a-g) Phase diagrams of the other seven XDESs. (h) The thermal behavior of $(TEAC)_{0.5}(IBr)_{0.5}$ in successive cycles. Blue and red lines represent the first and second heating cycles, respectively.

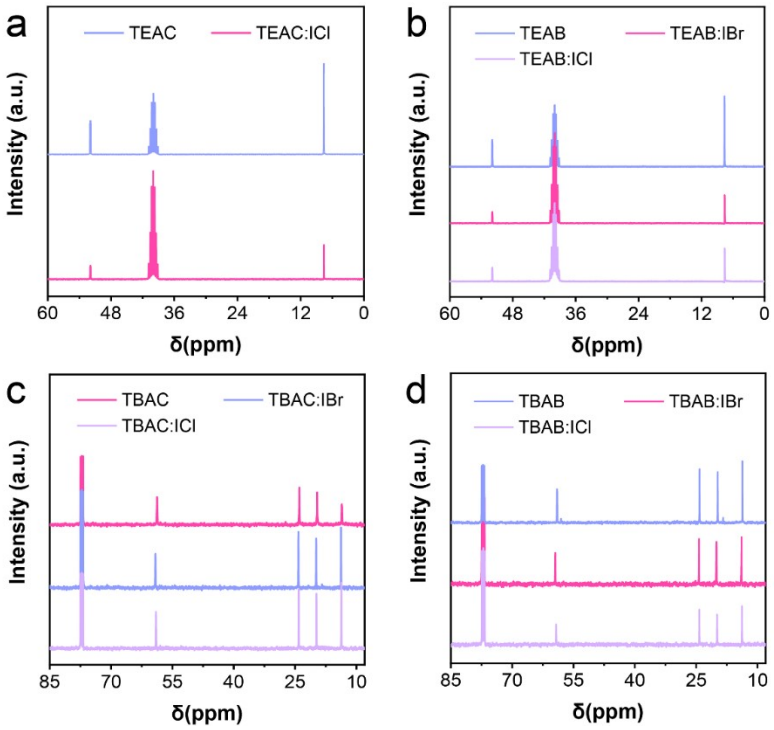

Fig. S4. (a-b) The ^{13}C NMR spectra of pure TEAC, TEAB and corresponding XDESs

at eutectic point. The solvent is DMSO-d_6. (c-d) ^{13}C NMR spectra of pure TBAC, TBAB and XDESs at respective eutectic points. The solvent is $CDCl_3$.

NMR spectroscopy, as an effective technique, have been widely utilized to study the weak interactions overall. In this work, the ^{13}C NMR spectroscopy was applied to further elucidate the interactions between quaternary ammonium salts and IBr/ICl. As shown in Fig. S4, the characteristic peaks of these XDES systems are roughly consistent with the pure XBA components indicating there are only noncovalent interactions. In detail, there are barely peak shifts in the TEAC/TEAB-based XDESs, but the characteristic peaks show a little change in TBAC/TBAB XDESs as follows. This might be exist additional HB interactions due to the increasement of alkyl chains. In short, there are only noncovalent interactions between donor and acceptor parts of XDESs

TEAC: ^{13}C NMR (101 MHz, DMSO-d_6) δ 51.51, 40.43, 40.16, 39.88, 39.60, 39.32, 39.04, 38.76, 7.25
TEAC+IBr: ^{13}C NMR (101 MHz, DMSO-d_6) δ 51.53, 40.43, 40.16, 39.88, 39.60, 39.32, 39.04, 38.76, 7.18
TEAC+ICl: ^{13}C NMR (101 MHz, DMSO-d_6) δ 51.51, 40.43, 40.16, 39.88, 39.60, 39.32, 39.04, 38.76, 7.12
TEAB: ^{13}C NMR (101 MHz, DMSO-d_6) δ 51.54, 40.43, 40.16, 39.88, 39.60, 39.32, 39.04, 38.76, 7.22
TEAB+IBr: ^{13}C NMR (101 MHz, DMSO-d_6) δ 51.54, 40.43, 40.16, 39.88, 39.60, 39.32, 39.04, 38.76, 7.20
TEAB+ICl: ^{13}C NMR (101 MHz, DMSO-d_6) δ 51.52, 40.43, 40.16, 39.88, 39.60, 39.32, 39.04, 38.76, 7.17
TBAC: ^{13}C NMR (101 MHz, $CDCl_3$) δ 77.49, 77.17, 76.85, 58.80, 24.00, 19.64, 13.68

TBAC+IBr: ^{13}C NMR (101 MHz, $CDCl_3$) δ 77.49, 77.17, 76.85, 59.19, 24.22, 19.89, 13.80
TBAC+ICl: ^{13}C NMR (101 MHz, $CDCl_3$) δ 77.49, 77.17, 76.85, 59.04, 24.14, 19.81, 13.73
TBAB: ^{13}C NMR (101 MHz, $CDCl_3$) δ 77.49, 77.17, 76.85, 59.05, 24.12, 19.77, 13.71

TBAB+IBr: ^{13}C NMR (101 MHz, $CDCl_3$) δ 77.49, 77.17, 76.85, 59.53, 24.37, 20.12, 13.98

TBAB+ICl: ^{13}C NMR (101 MHz, $CDCl_3$) δ 77.49, 77.17, 76.85, 59.34, 24.33, 19.98, 13.88

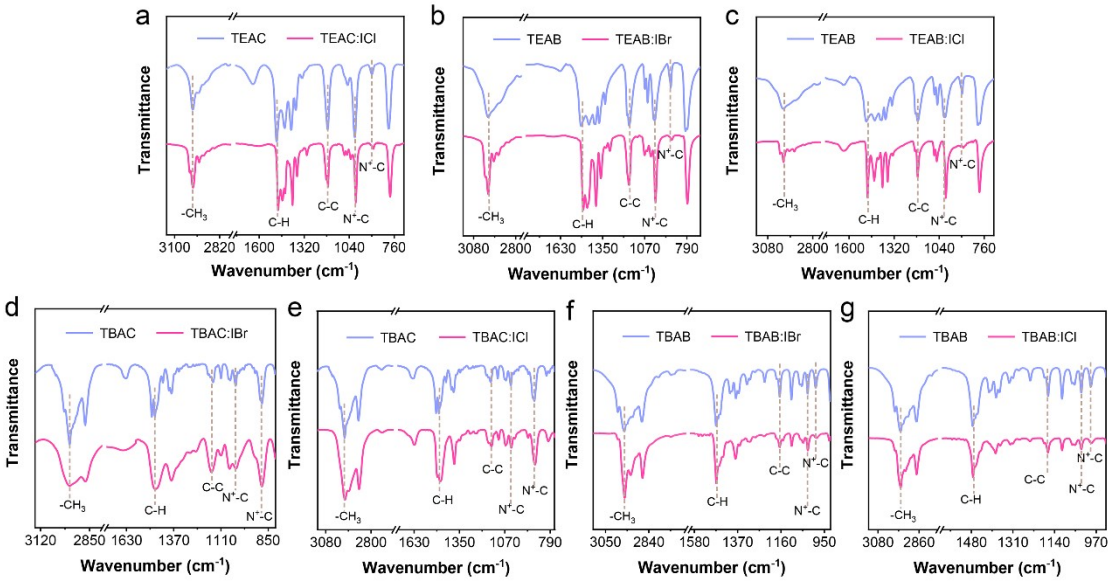

Fig. S5. (a-g) The FTIR spectra of other seven XDESs (at respective eutectic points) and corresponding pure components.

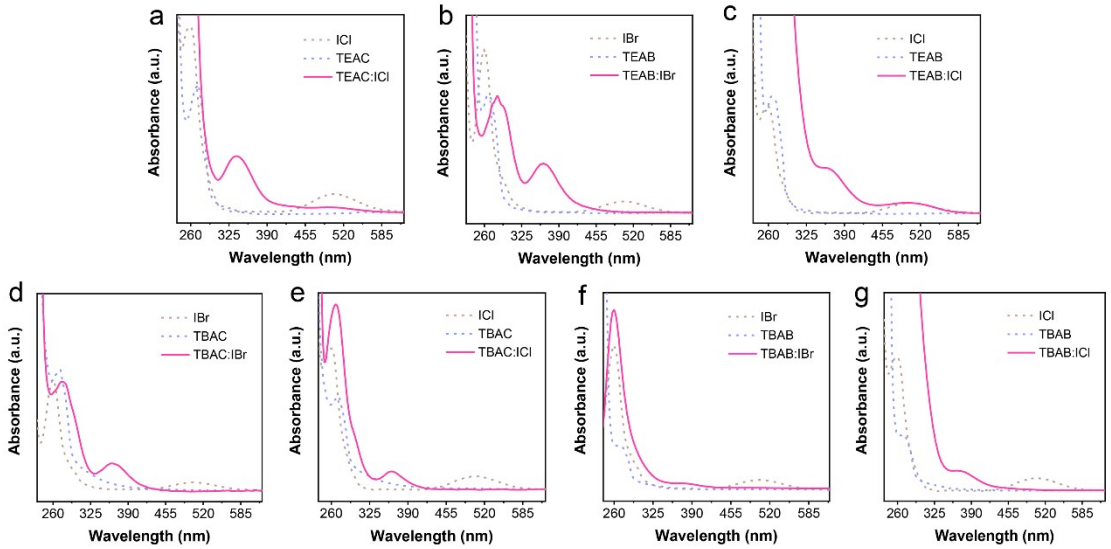

Fig. S6. (a-g) The UV-vis spectrum of other seven XDESs (at respective eutectic points) and corresponding pure components. The solvent is CH_2Cl_2.

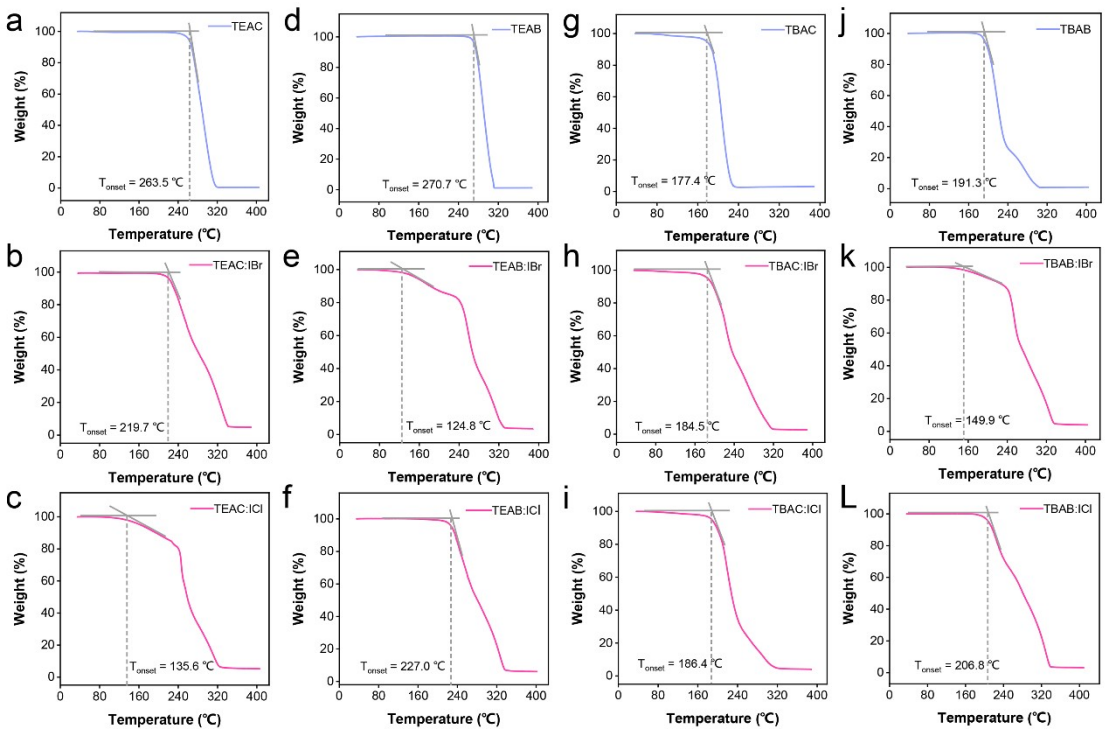

Fig. S7. TGA curves of XBD components and the XDESs systems (at respective eutectic points).

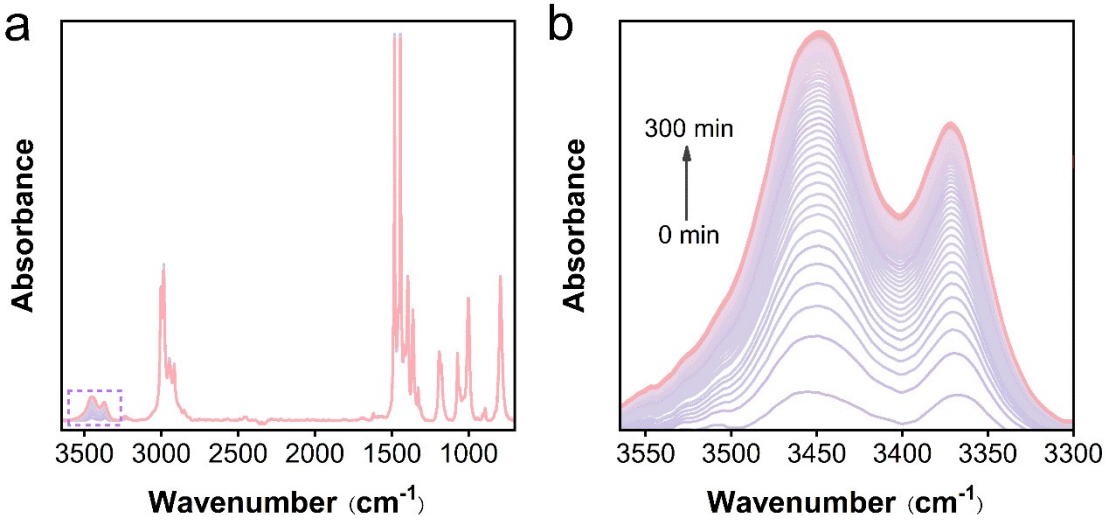

Fig. S8. (a) Dynamic IR spectra of $(TEAC)_{0.5}(IBr)_{0.5}$ XDES. This XDES evaporates

under 1 atm, 25 ℃. From down to up correspond to the time from 0 to 300 min with an interval of 4 min. The part of dashed box presents the region of markedly varied water peaks and the corresponding enlarged image is shown in (b).

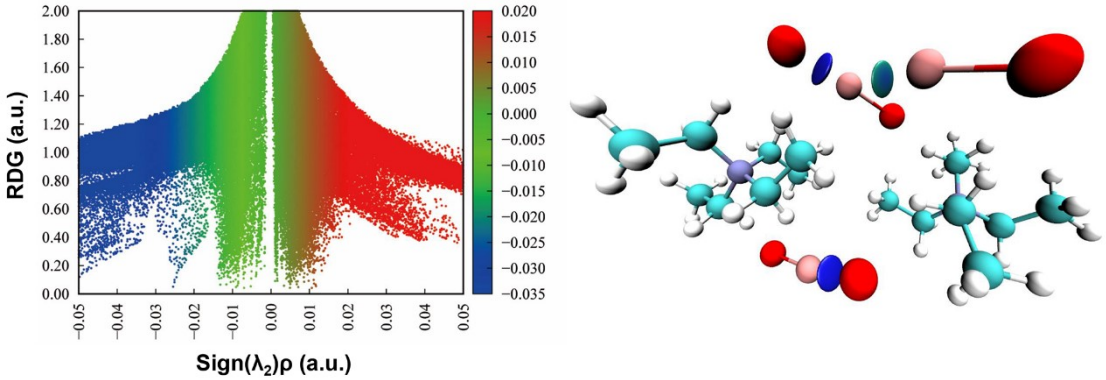

Fig. S9. Plot of the reduced density gradient (RDG) versus the electron density multiplied by the sign of the second Hessian eigenvalue ($\text{sign}(\lambda_2)\rho$) (left) and corresponding gradient isosurfaces for $(TEAC)_{0.4}(ICl)_{0.6}$ XDES.

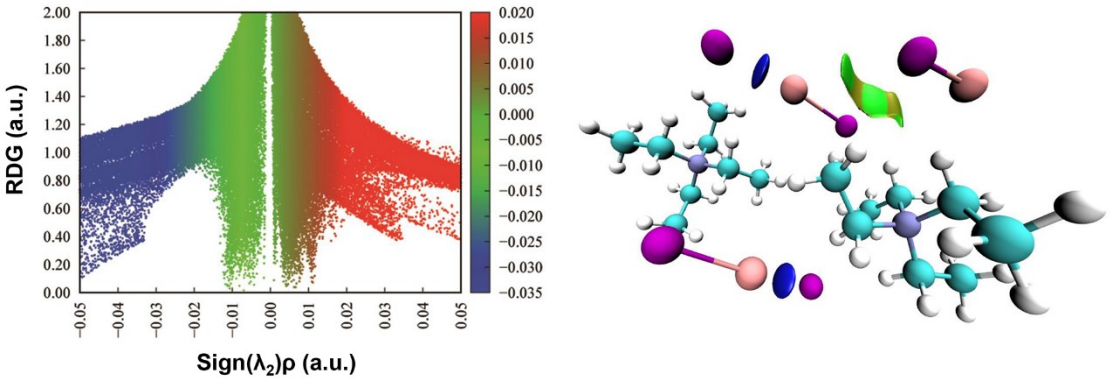

Fig. S10. Plot of the reduced density gradient (RDG) versus the electron density multiplied by the sign of the second Hessian eigenvalue ($\text{sign}(\lambda_2)\rho$) (left) and corresponding gradient isosurfaces for $(TEAB)_{0.4}(IBr)_{0.6}$ XDES.

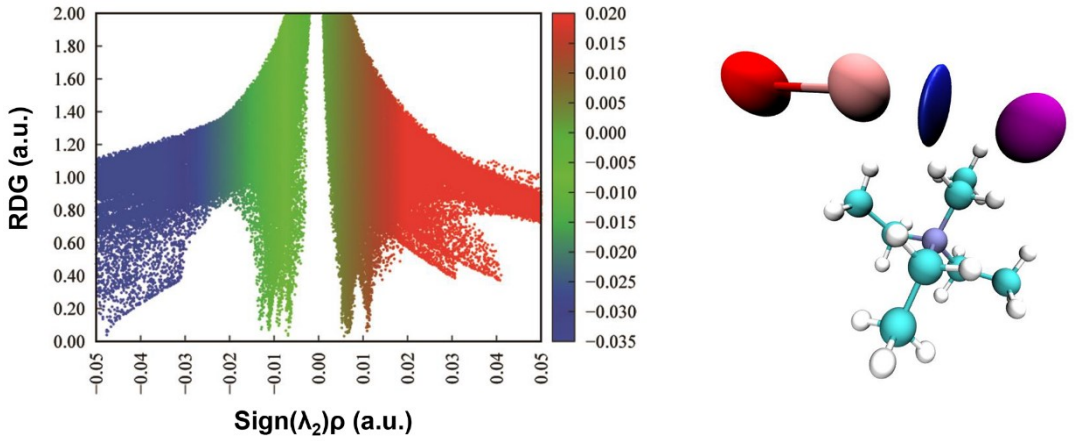

Fig. S11. Plot of the reduced density gradient (RDG) versus the electron density multiplied by the sign of the second Hessian eigenvalue (sign(λ_2)ρ) (left) and corresponding gradient isosurfaces for $(TEAB)_{0.5}(ICl)_{0.5}$ XDES.

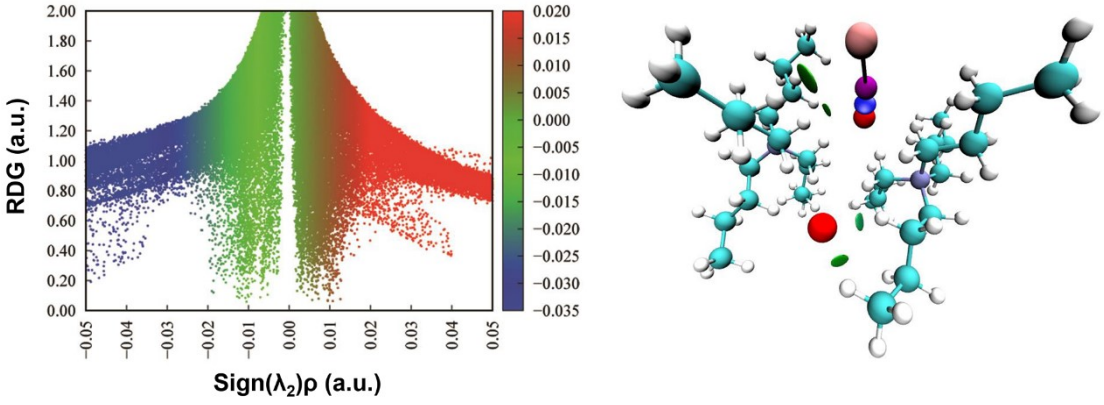

Fig. S12. Plot of the reduced density gradient (RDG) versus the electron density multiplied by the sign of the second Hessian eigenvalue (sign(λ_2)ρ) (left) and corresponding gradient isosurfaces for $(TBAC)_{0.67}(IBr)_{0.33}$ XDES.

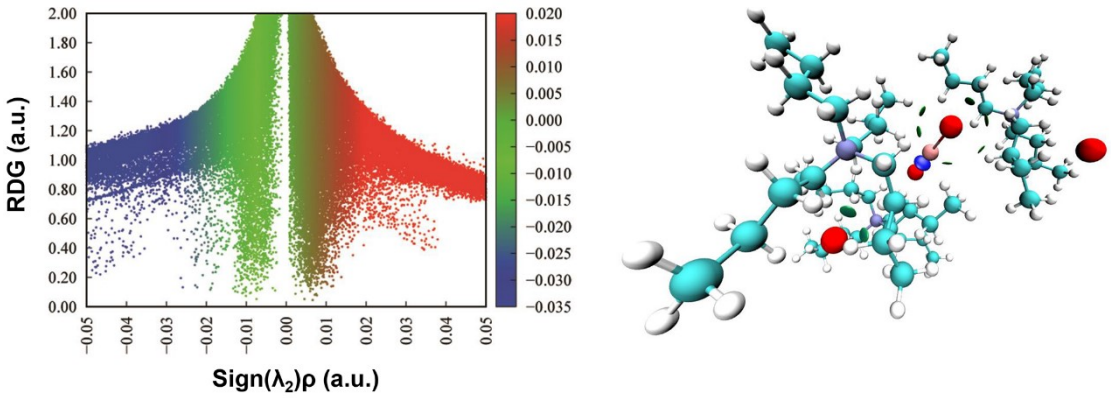

Fig. S13. Plot of the reduced density gradient (RDG) versus the electron density multiplied by the sign of the second Hessian eigenvalue (sign(λ_2)ρ) (left) and corresponding gradient isosurfaces for $(TBAC)_{0.75}(ICl)_{0.25}$ XDES.

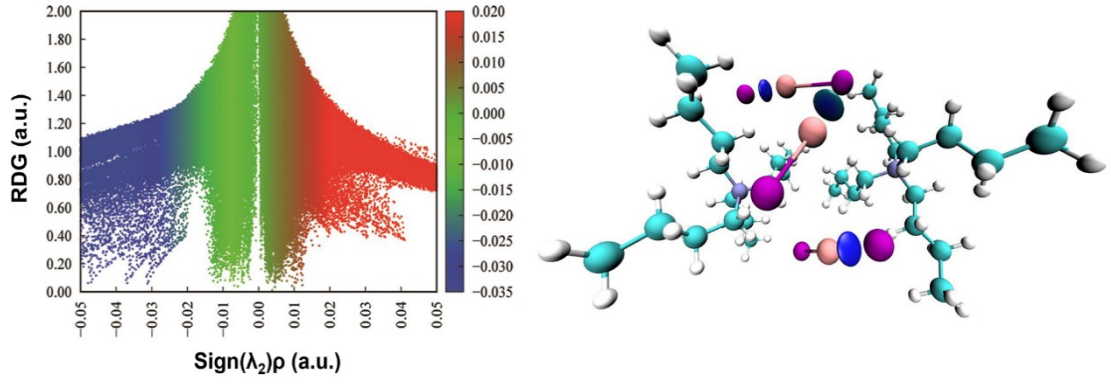

Fig. S14. Plot of the reduced density gradient (RDG) versus the electron density multiplied by the sign of the second Hessian eigenvalue (sign(λ_2)ρ) (left) and corresponding gradient isosurfaces for $(TBAB)_{0.4}(IBr)_{0.6}$ XDES.

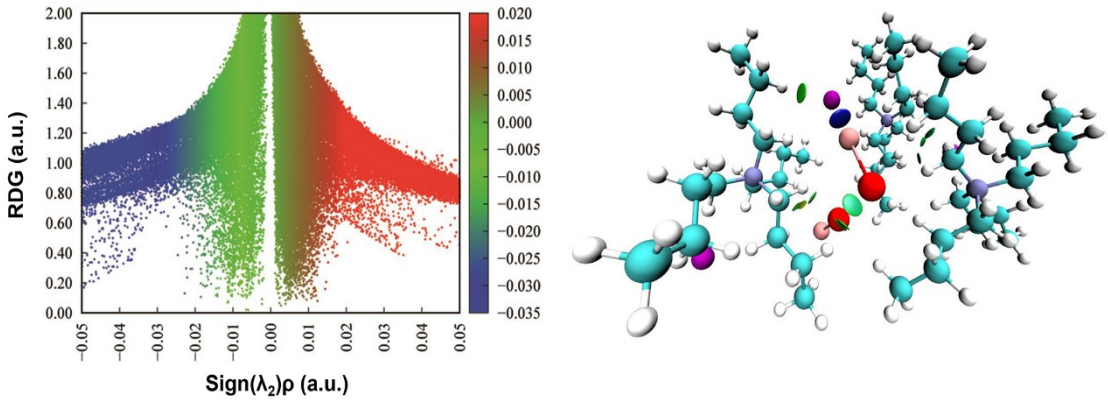

Fig. S15. Plot of the reduced density gradient (RDG) versus the electron density multiplied by the sign of the second Hessian eigenvalue ($sign(\lambda_2)\rho$) (left) and corresponding gradient isosurfaces for $(TBAB)_{0.6}(ICl)_{0.4}$ XDES.

There are additional weak HB interactions marked with blue-green disc-like isosurface when the molar ratio of quaternary ammonium salts are more than dihalogen molecules which might be due to the relatively large number of alkyl groups. Besides, some XDES systems display a vdW type interaction on account of polarization effect shown with a green-yellow isosurface. On the whole, the trihalide anions formed by the strong XB interactions dominate in all XDES systems in this work.

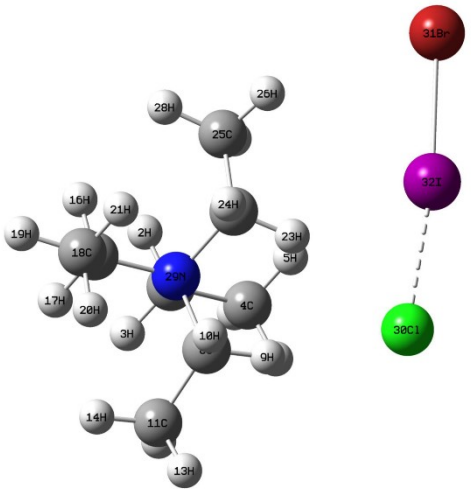

E_{int} = -25.10 kcal/mol

Fig. S16. A diagram of optimized geometries of TEAC-IBr complex at the eutectic molar ratio. The halogen bond was marked with dash lines and the interaction energy was provided.

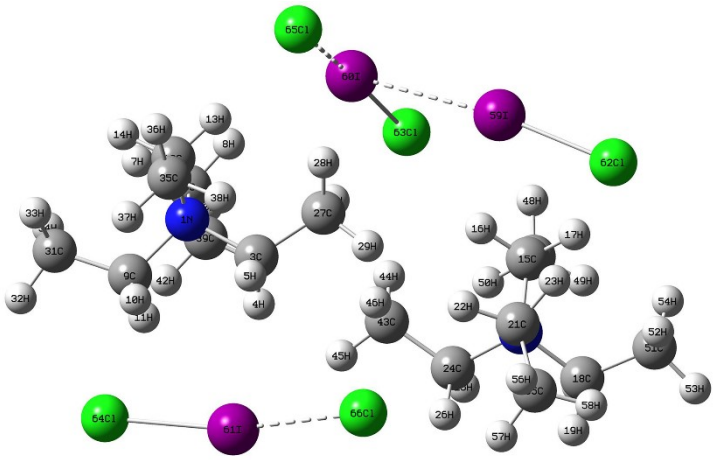

E_{int} = -106.68 kcal/mol

Fig. S17. A diagram of optimized geometries of TEAC-ICl complex at the eutectic molar ratio. The halogen bonds were marked with dash lines and the interaction energy was provided.

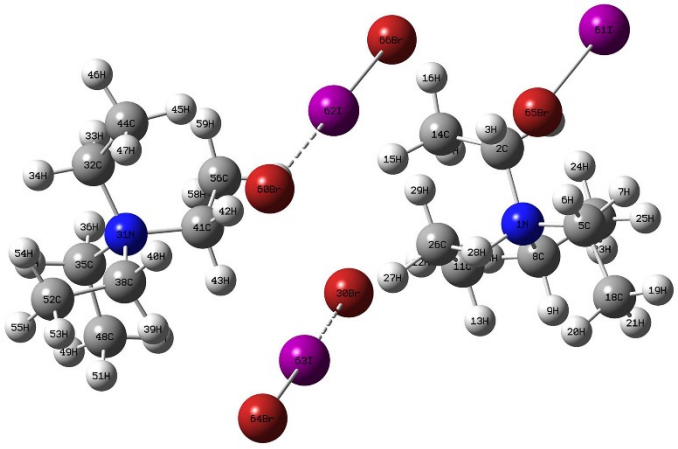

E_{int} = -87.85 kcal/mol

Fig. S18. A diagram of optimized geometries of TEAB-IBr complex at the eutectic molar ratio. The halogen bonds were marked with dash lines and the interaction energy

was provided.

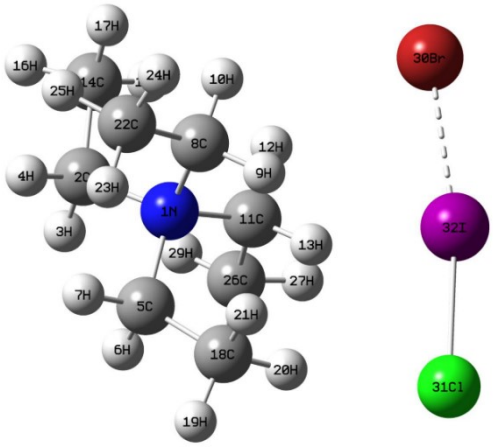

Fig. S19. A diagram of optimized geometries of TEAB-ICl complex at the eutectic molar ratio. The halogen bond was marked with dash lines and the interaction energy was provided.

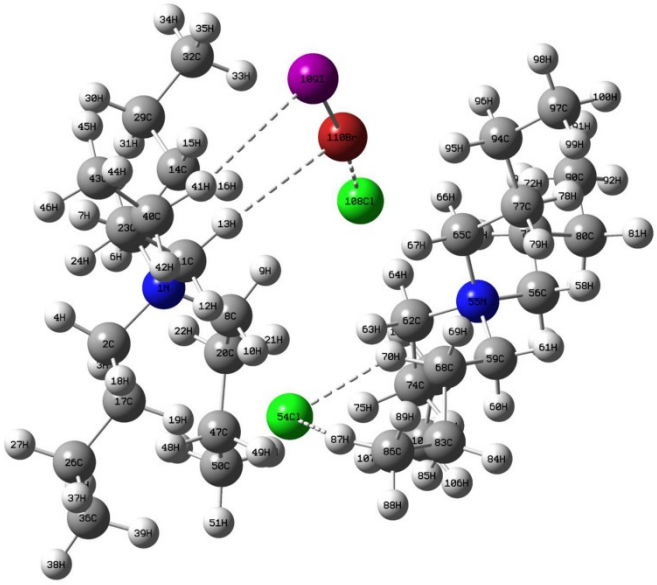

E_{int} = -62.75 kcal/mol

Fig. S20. A diagram of optimized geometries of TBAC-IBr complex at the eutectic molar ratio. The halogen bond and hydrogen bonds were marked with dash lines and the interaction energy was provided.

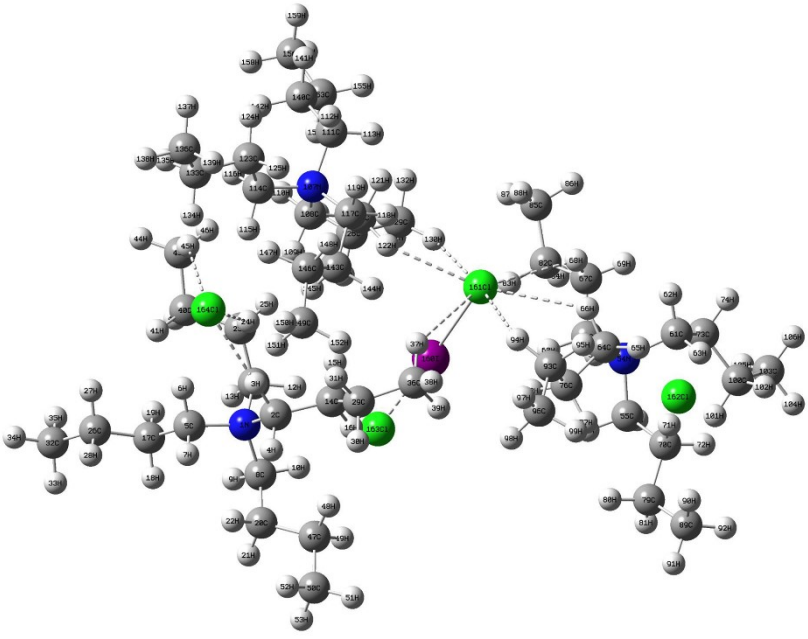

E_{int} = -81.58 kcal/mol

Fig. S21. A diagram of optimized geometries of TBAC-ICl complex at the eutectic molar ratio. The halogen bond and hydrogen bonds were marked with dash lines and

the interaction energy was provided.

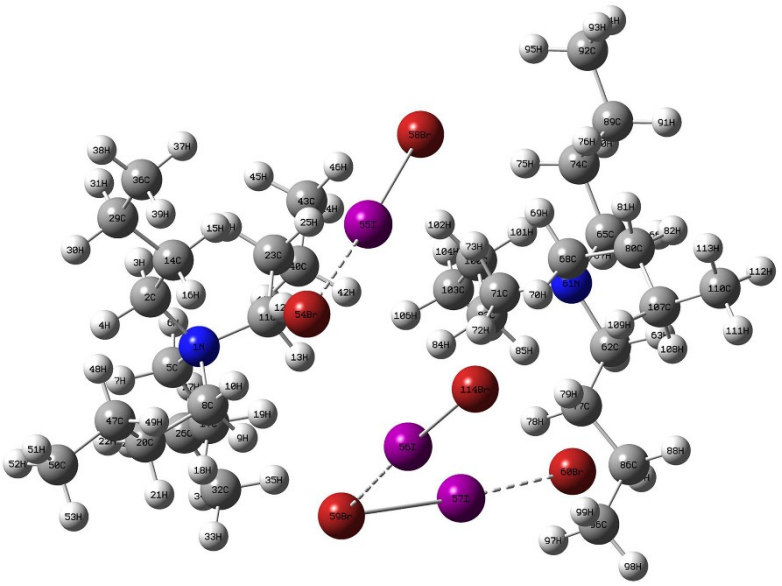

Fig. S22. A diagram of optimized geometries of TBAB-IBr complex at the eutectic molar ratio. The halogen bonds were marked with dash lines and the interaction energy was provided.

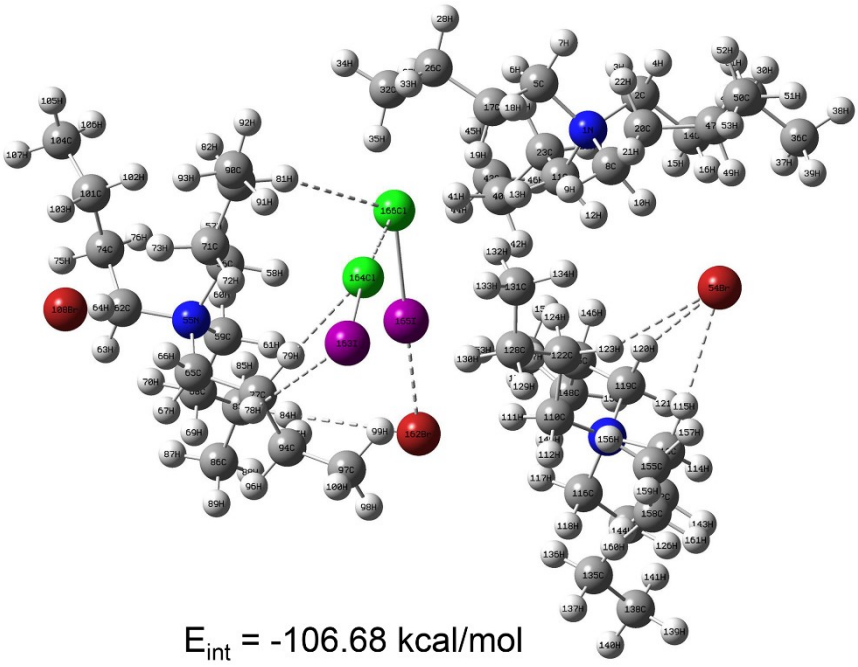

Fig. S23. A diagram of optimized geometries of TBAB-ICl complex at the eutectic molar ratio. The halogen bonds and hydrogen bonds were marked with dash lines and

the interaction energy was provided.

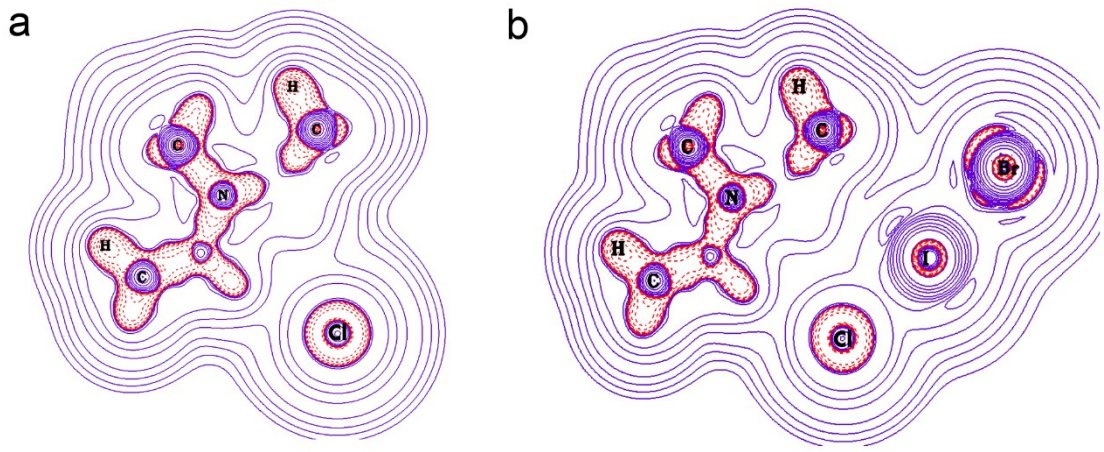

Fig. S24. The 2D contour maps of the Laplacian of the electron density ($\nabla^2\rho$) for XB acceptor TEAC (a) and $(TEAC)_{0.5}(IBr)_{0.5}$ system (b). The red dash line and purple solid line correspond to the negative and positive zone, respectively. Computational level: M06-2X/def2-SVP.

In comparison with pure TEAC, the positive electron density distribution around the Cl atom decreases after the formation of complex. Simultaneously, the electron density around I atom is more than pure IBr (Fig. S1a) showing the existence of intermolecular interaction between I and Cl atoms.

3. Table

Table S1. IR spectral peaks of pure XB acceptors and prepared XDESs (at respective eutectic points). The value given is corresponding to the peak absorbance of pure components.

Substrate/System	$\nu_{(N^+-C),}$ cm^{-1}
TEAC	1008, 902
TEAC+IBr	991, 902
TEAC+ICl	995, 889
TEAB	1006, 898
TEAB+IBr	995, 885
TEAB+ICl	1001, 889
TBAC	1031, 885
TBAC+IBr	1024, 883
TBAC+ICl	1024, 877
TBAB	1029, 991
TBAB+IBr	1027, 985
TBAB+ICl	1027, 989

Table S2. Some topological properties in a.u at the bond critical point (bcp) of the XB interaction between TEAC and IBr in the $(TEAC)_{0.5}(IBr)_{0.5}$ XDES obtained using the atoms in molecules (AIM) theory by the M06-2X/def2-SVP method. The numberings of the atoms in Table S2 are the same as the Fig. S16.

type	ρ_{bcp}[a] (10^{-2})	$\nabla^2\rho_{bcp}$[b] (10^{-2})	H_{bcp}[c] (10^{-2})	V_{bcp}[d] (10^{-2})	E[e]	L[f]	R[g]	θ[h]
Br31−I32···Cl¯30	4.8	7.9	-0.72	-3.4	-9.97	2.68	0.71	172.6

[a] The electron density. [b] The Laplacian of electron density. [c] The energy density.

[d] The potential electron density. [e] The bond energy, kcal/mol. [f] The bond length, Å.

[g] $R = \frac{L_{(I\cdots Cl^-)}}{(r_I + r_{Cl^-})}$ where r_I and r_{Cl^-} are *van der* Waals radii of iodine and Pauling ionic radii of chlorine, respectively.

[h] The bond angle, deg.

Table S3. Some topological properties in a.u at the bond critical points (bcps) of the XB interactions between TEAC and ICl in the $(TEAC)_{0.4}(ICl)_{0.6}$ XDES obtained using the atoms in molecules (AIM) theory by the M06-2X/def2-SVP method. The numberings of the atoms in Table S3 are the same as the Fig. S17.

type	ρ_{bcp} (10^{-2})	$\nabla^2\rho_{bcp}$ (10^{-2})	H_{bcp} (10^{-3})	V_{bcp} (10^{-2})	E	L	R	θ
Cl63−I60···Cl¯65	6.1	8.4	-13	-4.6	-12.87	2.56	0.68	175.3
Cl64−I61···Cl¯66	5.2	8.4	-8.9	-3.9	-10.86	2.63	0.70	167.9
Cl62−I59···I60−Cl63	2.6	5.2	-0.088	-1.3	-5.06	3.21	0.81	168.7/ 85.2

Table S4. Some topological properties in a.u at the bond critical points (bcps) of the XB interactions between TEAB and IBr in the $(TEAB)_{0.4}(IBr)_{0.6}$ XDES obtained using the atoms in molecules (AIM) theory by the M06-2X/def2-SVP method. The numberings of the atoms in Table S4 are the same as the Fig. S18.

type	ρ_{bcp} (10^{-2})	$\nabla^2\rho_{bcp}$ (10^{-2})	H_{bcp} (10^{-3})	V_{bcp} (10^{-2})	E	L	R	θ
Br66−I62···Br¯60	5.4	6.4	-9.9	-3.6	-11.30	2.74	0.69	174.4
Br64−I63···Br¯30	5.1	6.5	-8.6	-3.3	-10.63	2.74	0.70	175.7

Table S5. Some topological properties in a.u at the bond critical point (bcp) of the XB interaction between TEAB and ICl in the $(TEAB)_{0.5}(ICl)_{0.5}$ XDES obtained using the atoms in molecules (AIM) theory by the M06-2X/def2-SVP method. The numberings

of the atoms in Table S5 are the same as the Fig. S19.

type	ρ_{bcp} (10^{-2})	$\nabla^2\rho_{bcp}$ (10^{-2})	H_{bcp} (10^{-3})	V_{bcp} (10^{-2})	E	L	R	θ
Cl31−I32···Br¯30	4.8	6.6	-7.2	-3.1	-9.97	2.78	0.71	170.4

Table S6. Some topological properties in a.u at the bond critical points (bcps) of the XB and HB interactions between TBAC and IBr in the $(TBAC)_{0.67}(IBr)_{0.33}$ XDES obtained using the atoms in molecules (AIM) theory by the M06-2X/def2-SVP method. The numberings of the atoms in Table S6 are the same as the Fig. S20.

type	ρ_{bcp} (10^{-2})	$\nabla^2\rho_{bcp}$ (10^{-2})	H_{bcp} (10^{-3})	V_{bcp} (10^{-2})	E	L	R	θ
I109−Br110···Cl¯108	5.4	10.0	-5.3	-3.6	-11.30	2.55	0.71	174.1
C11−H13…Br110	0.71	1.9	0.35	-0.41	-0.84	3.03	0.99	164.9
C40−H41…I109	0.63	1.6	0.58	-0.29	-0.66	3.24	1.02	155.2
C68−H70…Cl¯54	1.7	4.0	-0.84	-1.2	-3.05	2.51	0.85	139.8
C86−H87…Cl¯54	0.85	2.5	0.47	-0.52	-1.15	2.88	0.98	130.5

Table S7. Some topological properties in a.u at the bond critical points (bcps) of the XB and HB interactions between TBAC and ICl in the $(TBAC)_{0.75}(ICl)_{0.25}$ XDES obtained using the atoms in molecules (AIM) theory by the M06-2X/def2-SVP method. The numberings of the atoms in Table S7 are the same as the Fig. S21.

type	ρ_{bcp} (10^{-2})	$\nabla^2\rho_{bcp}$ (10^{-2})	H_{bcp} (10^{-3})	V_{bcp} (10^{-2})	E	L	R	θ
Cl161−I160…Cl¯163	6.1	8.5	-12.0	-4.6	-12.87	2.55	0.67	176.1
C2−H3…Cl¯164	1.9	4.3	-1.2	-1.3	-3.50	2.42	0.82	169.8
C23−H24…Cl¯164	1.9	4.5	-1.1	-1.3	-3.50	2.45	0.83	144.1
C36−H37…Cl161	0.76	2.3	0.49	-0.48	-0.95	2.92	0.99	139.3
C43−H45…Cl¯164	1.0	2.7	0.16	-0.64	-1.49	2.80	0.95	134.7
C64−H66…Cl161	0.82	2.7	0.71	-0.53	-1.09	2.89	0.98	124.8

C67−H68…Cl161	1.1	3.5	0.74	-0.72	-1.71	2.76	0.94	114.7
C93−H94…Cl161	0.66	2.2	0.72	-0.40	-0.73	2.99	1.01	127.4
C120−H122…Cl161	1.2	3.1	-0.26	-0.83	-1.93	2.66	0.90	143.3
C129−H130…Cl161	1.1	2.9	-0.041	-0.73	-1.71	2.73	0.93	150.0

Table S8. Some topological properties in a.u at the bond critical points (bcps) of the XB between TBAB and IBr in the $(TBAB)_{0.4}(IBr)_{0.6}$ XDES obtained using the atoms in molecules (AIM) theory by the M06-2X/def2-SVP method. The numberings of the atoms in Table S8 are the same as the Fig. S22.

type	ρ_{bcp} (10^{-2})	$\nabla^2\rho_{bcp}$ (10^{-2})	H_{bcp} (10^{-3})	V_{bcp} (10^{-2})	E	L	R	θ
Br58−I55…Br¯54	5.6	6.3	-11.0	-3.8	-11.75	2.69	0.68	173.6
Br59−I57…Br¯60	6.5	5.7	-16.0	-4.6	-13.75	2.62	0.67	173.5
Br114−I56…Br59−I57	3.1	6.2	-1.4	-1.8	-6.17	2.99	0.78	171.0/85.4

Table S9. Some topological properties in a.u at the bond critical points (bcps) of the XB and HB interactions between TBAB and ICl in the $(TBAB)_{0.6}(ICl)_{0.4}$ XDES obtained using the atoms in molecules (AIM) theory by the M06-2X/def2-SVP method. The numberings of the atoms in Table S9 are the same as the Fig. S23.

type	ρ_{bcp} (10^{-2})	$\nabla^2\rho_{bcp}$ (10^{-2})	H_{bcp} (10^{-3})	V_{bcp} (10^{-2})	E	L	R	θ
Cl166−I165…Br¯162	5.6	6.4	-11.0	-3.8	-11.75	2.70	0.70	178.5
I163−Cl164…Cl166−I165	1.8	5.1	0.09	-1.3	-3.27	3.02	0.86	171.0/85.4
C77−H78…I163	0.54	1.6	0.83	-0.23	-0.46	3.34	1.05	116.1
C77−H79…Cl164	1.2	3.1	-0.22	-0.81	-1.93	2.67	0.91	151.1
C80−H81…Cl166	0.66	2.0	0.51	-0.39	-0.73	2.98	1.01	156.4
C83−H84…Br¯l62	0.76	1.9	0.26	-0.42	-0.95	2.99	0.98	177.1
C113−H115…Br¯54	1.4	3.1	-0.39	-0.85	-2.38	2.67	0.88	162.2

C119−H120…Br¯54	1.7	3.7	-0.55	-10.0	-3.05	2.57	0.84	159.6
C122−H123…Br¯54	1.1	2.7	0.052	-0.67	-1.71	2.83	0.93	136.7

The bond energy (E) is also an important parameter to characterize the non-covalent bond strength. Here, we adopted the current more reliable and universal calculation for predict the H-bond and X-bond binding energy based on electron density at corrsponding BCP[13]:

$$E \approx -223.08 \times \rho(r_{BCP}) + 0.7423$$

The nature of H-bonds/X-bonds in the complexes are classified according to the following report by Rozas et al.[14]:

1) weak: $\nabla^2\rho_{bcp} > 0$ and $H_{bcp} > 0$,

2) medium: $\nabla^2\rho_{bcp} > 0$ and $H_{bcp} < 0$, and

3) strong: $\nabla^2\rho_{bcp} < 0$ and $H_{bcp} < 0$.

Firstly, the values of electron density (ρ_{bcp}) and Laplacian of electron density ($\nabla^2\rho_{bcp}$) are both in the criteria range[15] confirm the existence of XB interaction in all complex. Secondly, the XB and HB interactions in prepared complexes all belong to closed-shell interactions[16]. Then, in terms of the classification criteria, the X-bonds in all prepared XDESs are medium strong and most of the contained H-bonds are weak.

Table S10. The values of bond distance and |V|/G ratio for trihalide anions of prepared XDESs (X1−X2: dihalogen; Y¯: halide anion of quaternary ammonium salt; V: the potential energy density; G: the kinetic energy density at the bond critical point (BCP)).

XDES	Trihalide anion	$L_{X2\text{-}X1}$ (Å)	$L_{X1\cdots Y^-}$ (Å)	|V|/G
$(TEAC)_{0.5}(IBr)_{0.5}$	Br31−I32⋯Cl¯30	2.64	2.68	1.26
$(TEAC)_{0.4}(ICl)_{0.6}$	Cl63−I60⋯Cl¯65	2.54	2.56	1.39
	Cl64−I61⋯Cl¯66	2.53	2.63	1.30
$(TEAB)_{0.4}(IBr)_{0.6}$	Br66−I62⋯Br¯60	2.74	2.72	1.38
	Br64−I63⋯Br¯30	2.71	2.74	1.32
$(TEAB)_{0.5}(ICl)_{0.5}$	Cl31−I32⋯Br¯30	2.53	2.78	1.26

$(TBAC)_{0.67}(IBr)_{0.33}$	I109−Br110···Cl^{-}108	2.67	2.54	1.16
$(TBAC)_{0.75}(ICl)_{0.25}$	Cl161−I160···Cl^{-}163	2.61	2.55	1.35
$(TBAB)_{0.4}(IBr)_{0.6}$	Br58−I55···Br^{-}54	2.78	2.69	1.41
	Br59−I57···Br^{-}60	2.90	2.62	1.53
$(TBAB)_{0.6}(ICl)_{0.4}$	Cl166−I165···Br^{-}162	2.61	2.70	1.41

The trihalides include two systems, which one is the symmetrical arrangement and the other is asymmetrical arrangement. Among, the halogen bonding interaction of former belongs to the three-center-four-electron halogen bond, 3c4e, while the latter could be described as donor-acceptor complexes between X^{-} (donor) and X_2 (acceptor)[17, 18]. In this work, we will illustrate the asymmetry of trihalide anions in our prepared XDESs from the following two aspects:

i. The asymmetry could be estimated by seeing if bond distance and atomic radius are consistent. As shown in Table S10, the bond distance of X1−X2 and X1···Y^{-} are not basically consistent for all XDESs. And the case of discordant atomic radius also exists in the heteroatomic trihalide anion. Besides, the trihalide anions are often asymmetry in solution[19, 20]. Thus, we thought the formed-trihalide anions in XDESs are asymmetry.

ii. The covalent nature of a bond can be estimated by analyzing the |V|/G ratio of the bond. In pure electrostatic interactions the ratio is typically <1 and in pure covalent bonds two or more. The values between one and two are indicative to bonds with both electrostatic and covalent nature[21]. Hence, we used this method to judge the covalent nature of halogen bond in trihalide anion of XDES and the details are also listed in Table S10. These results shows that all halogen bonds between X2−X1 and Y^{-} have both electrostatic and covalent nature but they are not covalent bond (viz. 3c4e bond). And for the pure quaternary ammonium salts, the halide anions could be naked or firmly pinned in the coordination sphere of the cation[22], so the dihalogen could not completely take the halide anions away from the quaternary ammonium salts under the solution state to form the 3c4e bonded-trihalide anions.

Above all, the formation of trihalide anion in our work mainly caused by the electrostatic interaction and the covalent nature derives from the charge transfer from the halides anion to the σ* orbit of dihalogen molecule. All trihalides are asymmetrical

arrangement and thus our prepared XDESs belong to the donor-acceptor complexes. So, the trihalide anions formed by the strong XB interactions between dihalogens and quaternary ammonium salts are critical for the formation of XDES systems in this work.

4. References

1. R. Dennington, T. Keith and J. Millam, 2009.
2. M. J. Frisch, G. W. Trucks, H. B. Schlegel, G. E. Scuseria, M. A. Robb, J. R. Cheeseman, G. Scalmani, V. Barone, B. Mennucci, G. A. Petersson, H. Nakatsuji, M. Caricato, X. Li, H. P. Hratchian, A. F. Izmaylov, J. Bloino, G. Zheng, J. L. Sonnenberg, M. Hada, M. Ehara, K. Toyota, R. Fukuda, J. Hasegawa, M. Ishida, T. Nakajima, Y. Honda, O. Kitao, H. Nakai, T. Vreven, J. A. J. Montgomery, J. E. Peralta, F. Ogliaro, M. Bearpark, J. J. Heyd, E. Brothers, K. N. Kudin, V. N. Staroverov, T. Keith, R. Kobayashi, J. Normand, K. Raghavachari, A. Rendell, J. C. Burant, S. S. Iyengar, J. Tomasi, M. Cossi, N. Rega, J. M. Millam, M. Klene, J. E. Knox, J. B. Cross, V. Bakken, C. Adamo, J. Jaramillo, R. Gomperts, R. E. Stratmann, O. Yazyev, A. J. Austin, R. Cammi, C. Pomelli, J. W. Ochterski, R. L. Martin, K. Morokuma, V. G. Zakrzewski, G. A. Voth, P. Salvador, J. J. Dannenberg, S. Dapprich, A. D. Daniels, O. Farkas, J. B. Foresman, J. V. Ortiz and J. Cioslowski, *Wallingford, CT*, 2009, **32**, 5648-5652.
3. F. Neese and E. F. Valeev, *J. Chem. Theory Comput.*, 2011, **7**, 33-43.
4. T. Lu and F. Chen, *J. Comput. Chem.*, 2012, **33**, 580-592.
5. W. Humphrey, A. Dalke and K. Schulten, *J. Mol. Graphics*, 1996, **14**, 33-38.
6. P. Politzer, J. S. Murray and T. Clark, *J. Phys. Chem. A*, 2019, **123**, 10123-10130.
7. B. Pinter, N. Nagels, W. A. Herrebout and F. De Proft, *Chem. Eur. J*, 2013, **19**, 518-529.
8. K. Eskandari and M. Lesani, *Chem. Eur. J*, 2015, **21**, 4739-4746.
9. K. Eskandari and N. Mahmoodabadi, *J. Phys. Chem. A*, 2013, **117**, 13018-13024.
10. P. Popelier, *Coord. Chem. Rev.*, 2000, **197**, 169-189.
11. L. Tian and C. Qinxue, *Acta Phys. -Chim. Sin.*, 2018, **34**, 503-513.
12. P. R. Varadwaj, A. Varadwaj, H. M. Marques and P. J. MacDougall, *Phys. Chem. Chem. Phys.*, 2019, **21**, 19969-19986.
13. S. Emamian, T. Lu, H. Kruse and H. Emamian, *J. Comput. Chem.*, 2019, **40**, 2868-2881.
14. I. Rozas, I. Alkorta and J. Elguero, *J. Am. Chem. Soc.*, 2000, **122**, 11154-11161.
15. U. Koch and P. L. A. Popelier, *J. Phys. Chem.*, 1995, **99**, 9747-9754.
16. H. Roohi, A.-R. Nowroozi and E. Anjomshoa, *Comput. Theor. Chem.*, 2011, **965**, 211-220.
17. F. F. Awwadi, D. Taher, M. H. Kailani, M. I. Alwahsh, F. Odeh, T. Rüffer, D. Schaarschmidt and H. Lang, *Crystal Growth & Design*, 2019, **20**, 543-551.
18. K. Sonnenberg, L. Mann, F. A. Redeker, B. Schmidt and S. Riedel, *Angew. Chem. Int. Ed. Engl.*, 2020, **59**, 5464-5493.

19. A. G. Maki and R. Forneris, *Spectrochim. Acta*, 1967, **23**, 867-880.
20. W. Gabes and H. Gerding, *J. Mol. Struct.*, 1972, **14**, 267-279.
21. E. Espinosa, I. Alkorta, J. Elguero and E. Molins, *J. Chem. Phys.*, 2002, **117**, 5529-5542.
22. G. Cavallo, P. Metrangolo, T. Pilati, G. Resnati, M. Sansotera and G. Terraneo, *Chem. Soc. Rev.*, 2010, **39**, 3772-3783.